Author(s): Jäger, Nikolaus; Meindlhumer, Michael; Zitek, Michal; Spor, Stefan; Hruby, Hynek; Nahif, Farwah; Julin, Jaakko; Rosenthal, Martin; Keckes, Jozef; Mitterer, Christian; Daniel, Rostislav

Title: Impact of Si on the high-temperature oxidation of AlCr(Si)N coatings

Year: 2022

Version: Published version

Please cite the original version:

Jäger, N., Meindlhumer, M., Zitek, M., Spor, S., Hruby, H., Nahif, F., Julin, J., Rosenthal, M., Keckes, J., Mitterer, C., & Daniel, R. (2022). Impact of Si on the high-temperature oxidation of AlCr(Si)N coatings. Journal of Materials Science and Technology, 100, 91-100. https://doi.org/10.1016/j.jmst.2021.04.065

Journal of Materials Science & Technology 100 (2022) 91–100

Contents lists available at ScienceDirect

Journal of Materials Science & Technology

journal homepage: www.elsevier.com/locate/jmst

Impact of Si on the high-temperature oxidation of AlCr(Si)N coatings

Nikolaus Jäger[a,*], Michael Meindlhumer[a], Michal Zitek[a], Stefan Spor[a,b], Hynek Hruby[b], Farwah Nahif[b], Jaakko Julin[c,d], Martin Rosenthal[e], Jozef Keckes[f,g], Christian Mitterer[g], Rostislav Daniel[a,g]

[a] Christian Doppler Laboratory for Advanced Synthesis of Novel Multifunctional Coatings at the Department of Materials Science, Montanuniversität Leoben, Austria
[b] voestalpine eifeler Vacotec GmbH, Düsseldorf, Germany
[c] Institute of Ion Beam Physics and Materials Research, Helmholtz-Zentrum Dresden-Rossendorf, Dresden, Germany
[d] Department of Physics, University of Jyvaskyla, Finland
[e] European Synchrotron Radiation Facility, Grenoble, France
[f] Erich Schmid Institute for Materials Science, Austrian Academy of Sciences, Austria
[g] Department of Materials Science, Montanuniversität Leoben, Austria

ARTICLE INFO

Article history:
Received 7 December 2020
Revised 10 March 2021
Accepted 3 April 2021
Available online 13 July 2021

Keywords:
AlCrSiN
Nanocomposite
Cathodic arc
Oxidation behaviour
Cross-sectional X-ray nanodiffraction

ABSTRACT

The resistance of wear protective coatings against oxidation is crucial for their use at high temperatures. Here, three nanocomposite AlCr(Si)N coatings with a fixed Al/Cr atomic ratio of 70/30 and a varying Si-content of 0 at.%, 2.5 at.% and 5 at.% were analyzed by differential scanning calorimetry, thermogravimetric analysis and X-ray in order to understand the oxidation behavior depending on their Si-content. Additionally, a partially oxidized AlCrSiN coating with 5 at.% Si on a sapphire substrate was studied across the coating thickness by depth-resolved cross-sectional X-ray nanodiffraction and scanning trans-mission electron microscopy to investigate the elemental composition, morphology, phases and residual stress evolution of the oxide scale and the non-oxidized coating underneath. The results reveal enhanced oxidation properties of the AlCr(Si)N coatings with increasing Si-content, as demonstrated by a retarded onset of oxidation to higher temperatures from 1100°C for AlCrN to 1260°C for the Si-containing coatings and a simultaneous deceleration of the oxidation process. After annealing of the AlCrSiN sample with 5 at.% Si at an extraordinary high temperature of 1400°C for 60 min in ambient air, three zones developed throughout the coating strongly differing in their composition and structure: (i) a dense oxide layer comprising an Al-rich and a Cr-rich zone formed at the very top, followed by (ii) a fine-grained transition zone with incomplete oxidation and (iii) a non-oxidized zone with a porous structure. The varying elemental composition of these zones is furthermore accompanied by micro-structural variations and a complex residual stress development revealed by cross-sectional X-ray nanodiffraction. The results provide a deeper understanding of the oxidation behavior of AlCr(Si)N coatings depending on their Si-content and the associated elemental, microstructural and residual stress evolution during high-temperature oxidation.

1. Introduction

Ceramic hard coatings are widely used in industry to protect the surface of tools in various machining and forming applications. Ternary transition metal nitrides find widespread use due to their good mechanical properties, thermal stability and oxidation resistance. However, modern applications like high-speed cutting or dry cutting demand for wear-protective coatings resisting high temperatures beyond 1000°C in oxidative atmospheres [1] and stimulate the development of superior coatings with advanced microstructural and compositional design.

AlCrN coatings are widely used in industry due to their high hardness, thermal stability and oxidation properties resulting in an overall good resistance against wear [2, 3, 4, 5]. The AlCrN system can be stabilized in its face-centered cubic structure up to an Al-content of about 70 at.% on the metal sublattice, and exhibits an additional hexagonal close packed phase exceeding this critical solubility limit [6]. As the cubic AlCrN phase is thermally metastable, it decomposes at elevated temperatures into hexagonal

* Corresponding author.
E-mail address: nikolaus.jaeger@stud.unileoben.ac.at (N. Jäger).

https://doi.org/10.1016/j.jmst.2021.04.065

Al(Cr)N and a Cr-enriched cubic Cr(Al)N phase [7]. In another step, c-Cr(Al)N decomposes into Cr_2N (and AlN) and finally Cr, accompanied by the release of nitrogen yielding a porous structure with undesirable mechanical properties [7, 8]. Several attempts have been made to stabilize the AlCrN system in its cubic structure also at high temperatures by alloying [9, 10], applying a multi-layered structure [11, 12] or using a dedicated residual stress design [13, 14].

Besides thermal stability, also the resistance against corrosion and oxidation is important as the coatings are often exposed to aggressive lubricants and coolants and face high temperatures in ambient air. Regarding oxidation, AlCrN is superior to CrN, resulting from the formation of an Al-rich oxide layer slowing down the diffusion of oxygen into the coating [15]. The oxidation behavior can be further improved by alloying using various elements [16, 17, 18, 19] including rare earth elements [19, 20], of which Si is a promising candidate [21]. The solubility of Si in AlCrN is below 1 at.% [22] and Si segregates along grain boundaries to form an amorphous (a-)Si_xN_y phase [23]. The resulting MeN/a-Si_xN_y (Me = Al/Cr) nanocomposite structure is beneficial for the oxidation resistance as no continuous diffusion path along grain boundaries exists and intergranular diffusion of oxygen is suppressed [24]. While AlCrSiN coatings have been investigated in terms of oxidation resistance or tribo-logical behavior in ambient air, a detailed study about the elemental and microstructural changes during high-temperature oxidation including the residual stress development and the properties after oxidation is still missing. In our previous work, we investigated the thermal stability of three AlCr(Si)N coatings excluding oxidation processes [25]. While the addition of Si resulted in a decrease in hardness from 32 GPa to 28 GPa in the as-deposited state of the coatings, the hardness after vacuum annealing at 1000°C was enhanced by the supplemental Si resulting in a hardness of 26 GPa and 29 GPa for AlCrN and both Si-containing coatings, respectively [25]. In this work, the same coatings (AlCr(Si)N coatings with a fixed Al/Cr atomic ratio of 70/30 and a Si-content of 0 at.%, 2.5 at.% and 5 at.%) were investigated in terms of oxidation behavior. In a first step, the coatings were analyzed by differential scanning calorimetry (DSC), thermogravimetric analysis (TA) and ex-situ X-ray diffraction (XRD) to understand the oxidation behavior as a function of Si-content. In a second step, the AlCrSiN coating with the highest oxidation resistance in the powdered state (5 at.% Si) was chosen to study the elemental and microstructural changes after high-temperature oxidation. For this purpose, the coating was partially oxidized by annealing it at 1400°C for 60 min in ambient air. Due to this extremely high annealing temperature, a thermally highly stable sapphire substrate was chosen to avoid interdiffusion of substrate and coating material. After oxidation, the sample comprising a 1.1 µm-thick oxide layer with a 3 µm-thick non-oxidized coating underneath was studied by depth-resolved cross-sectional X-ray nanodiffraction and scanning transmission electron microscopy (STEM).

The results reveal an increase of the onset of oxidation from 1100°C to 1260°C and a significantly slowed down oxidation for the AlCrSiN coatings compared to AlCrN. The beneficial oxidation behavior is mainly associated with a fundamental change in microstructure from columnar grains to a nanocomposite structure with an a-Si_xN_y grain boundary phase embedding AlCr(Si)N crystallites. A detailed depth-resolved analysis of the partially oxidized AlCrSiN sample with 5 at.% Si revealed the formation of a dense oxide layer comprising an Al-rich followed by a Cr-rich zone at the very top of the coating, a transition zone with incomplete oxidation and relatively fine grains comprising mainly mullite, SiO_2 and AlN underneath, and a non-oxidized coating with some pores closest to the substrate. The separation of the partially oxidized coating into zones with completely different elemental composition and microstructures is associated with the formation of different crystal phases and a fluctuating residual stress development across the coating thickness, as shown by cross-sectional X-ray nanodiffraction and STEM experiments. The approach comparing AlCr(Si)N coatings with varying Si-content using DSC/TG and ex-situ XRD combined with depth-resolved analysis of the partially oxidized AlCrSiN sample using advanced cross-sectional X-ray nanodiffraction and STEM allows for a comprehensive understanding of the oxidation behavior of AlCrSiN coatings and the underlying diffusion processes and changes in elemental composition, residual stress and microstructure.

2. Materials and methods

2.1. Coating deposition

Three AlCr(Si)N coatings with varying Si-contents were deposited by cathodic arc evaporation using an industrial scale coating system (alpha400P, voestalpine eifeler-Vacotec) equipped with sets of six cathodes with a fixed Al/Cr atomic ratio of 70/30 and an elemental composition of $Al_{70}Cr_{30}$, $Al_{66.5}Cr_{28.5}Si_5$ and $Al_{63}Cr_{27}Si_{10}$, respectively. The coatings were deposited onto WC-Co, polished sapphire substrates and on mild steel foil mounted in onefold planetary rotation with a turning speed of 2 rpm. Prior to the deposition, the substrates were heated and plasma-etched to remove contaminants and activate the surface to promote coating adhesion. For all coatings, a pure reactive nitrogen atmosphere with a pressure of 4 Pa, a substrate temperature of 480°C, an arc current on each cathode of 100 A and a substrate bias voltage of -100 V were used.

2.2. Coating characterization

While the oxidation behavior of all three coatings was analyzed by DSC and TG analysis and ex-situ XRD, the coating with the highest oxidation resistance deposited from the $Al_{63}Cr_{27}Si_{10}$ cathodes (denoted as $AlCrSi_5N$) was selected to study the elemental and microstructural changes depth-resolved along the coating cross-section after high-temperature oxidation. For this purpose, an $AlCrSi_5N$ sample on a sapphire substrate was oxidized at 1400°C for 60 min in ambient air, aiming for a partially oxidized sample consisting of a distinct oxide layer and a still preserved underlying coating.

Fracture cross-sections of all coatings in the as-deposited state were analyzed in terms of coating thickness and morphology using a scanning electron microscope (SEM) (Zeiss Leo1525, with 3 kV accelerating voltage, 30 µm aperture and an inLens detector). The elemental composition of the coatings in the as-deposited state were measured by Elastic Recoil Detection Analysis (ERDA) with a 43 MeV $^{35}Cl^{7+}$ ion beam. The analyzed area was approximately 1.5 mm x 1.5 mm, the angle of the incoming beam was 75° with respect to the sample normal and the scattering angle was 31° with respect to the beam. The recoiling atoms and scattered $^{35}Cl^{7+}$ ions were detected using a Bragg Ionization Chamber. Additionally, a cross-section of the partially oxidized $AlCrSi_5N$ coating was prepared by focused ion beam (FIB) microscopy in a ZEISS LEO 1540XB Crossbeam using decreasing currents from 500 pA to 20 pA for polishing while minimizing the Ga^+-ion damage. The sample was analyzed along the cross-section by energy dispersive X-ray spectroscopy (EDX) using 10 kV, a 60 µm aperture and the built-in Bruker Quantax standards for quantification. For DSC and TG analysis, the coated steel foil was chemically removed using 10 mol % nitric acid and the remaining coating material was ground in an agate mortar to obtain a fine powder. The DSC and TG experiments were carried out in synthetic air using a Setaram Setsys Evo 2400 system. 20 mg of each powdered sample was heated up to 1460°C using a heating rate of 20 K min^{-1} and cooled down at a cooling

Table 1
Elemental composition of the coatings obtained by ERDA.

Cathode composition	Coating composition [at.%/wt.%]				
	Al	Cr	Si	N	Al/Cr
$Al_{70}Cr_{30}$	32.6/35.7	16.7/35.3	0	51.0/29.0	2.0/1
$Al_{66.5}Cr_{28.5}Si_5$	32.6/36.8	14.0/30.5	2.6/3.1	50.6/29.7	2.3/1.2
$Al_{63}Cr_{27}Si_{10}$	30.8/34.9	13.7/29.9	4.7/5.5	50.5/29.7	2.2/1.2

rate of 50 K min^{-1} after an isothermal holding time of 30 min. A second run with an empty crucible was performed under the same conditions to serve as a baseline. Furthermore, additional samples (20 mg each) were annealed at 900°C, 1100°C, 1200°C, 1260°C, 1320°C and 1390°C, respectively, applying the same heating/cooling rates without isothermal holding. X-ray diffractograms of the annealed powders were recorded using a diffractometer (Bruker D8 Advance) equipped with an energy-dispersive Sol-X detector and applying Cu-K radiation (8.04 keV).

In order to gain depth-resolved information about the coating microstructure, phases, defect density and residual stress development across the coating thickness of the partially oxidized $AlCrSi_5N$, a 30 µm thick lamella (in beam direction) of the coating on a sapphire substrate (coating thickness of 4 µm) was investigated by cross-sectional synchrotron X-ray nanodiffraction [26] performed at the nanofocus extension of the ID13 beamline at the European Synchrotron Radiation Facility (ESRF) in Grenoble, France [27]. A monochromatic, point focusing X-ray beam (E = 12.7 keV) with dimensions of 25 nm x 35 nm adjusted by Multilayer Laue Lenses [28] was used in transmission geometry. The sample was moved along the whole coating thickness in steps of 20 nm and the diffraction data for each position were collected by a Dectris Eiger 4M detector. Detector calibration was performed by a NIST corundum powder and the sample-to-detector distance was evaluated as 134.927 mm. The resulting data were processed using the PyFAI software package [29, 30]. For every ring, 24 radial data sets were obtained by the azimuthal integration within 15° wide sections. The full width at half maximum (FWHM) values were evaluated by fitting the diffraction peaks using a Pseudo-Voigt function. The X-ray elastic stress depth distribution was received by analyzing the elliptical shape of the Debye-Scherrer rings [26]. The elastic constants 1/2 $s^{113}{}_2$ of 0.3252 × 10^{-5} MPa^{-1} for Al_2O_3, 1/2 $s^{113}{}_2$ of 0.4142 × 10^{-5} MPa^{-1} for Cr_2O_3 [31], 1/2 $s^{110}{}_2$ of 0.2848 × 10^{-5} MPa^{-1} for mullite [32] and 1/2 $s^{100}{}_2$ of 0.3903 × 10^{-5} MPa^{-1} for AlN [33] were used. All X-ray elastic constants were calculated using the Hill-type grain interaction model [34].

To study the microstructure and local variations in elemental composition of the individual regions of the partially oxidized $AlCrSi_5N$ coating, high resolution and analytical scanning transmission electron microscopy investigations were performed using a probe-corrected STEM (FEI Titan^3 G2 60-300) operated at 300 kV, equipped with a silicon drift detector X-ray spectrometer (Super-X). The sample for TEM were prepared by focused ion beam (Orsay Physics Cobra Z-05) column attached to a field emission gun scanning electron microscope (Zeiss Auriga).

3. Results

3.1. Elemental composition

The elemental composition of the coatings in the as-deposited state obtained by ERDA is reported already in [25] and given in Table 1 for completeness. The Al/Cr ratio of the coatings is slightly lower compared to the cathodes (Al/Cr = 2.3), revealing an Al loss during deposition due to preferred gas scattering of the lighter Al atoms within the plasma.

In contrast, the Si-content in the coatings corresponds to its content in the particular cathodes. The nitrogen content in all coatings is close to 50 at.% and the contamination with oxygen is below 0.4 at.% for all coatings. For easier reading, the coatings are denoted as AlCrN, $AlCrSi_{2.5}N$ and $AlCrSi_5N$ throughout the paper, corresponding to the $Al_{70}Cr_{30}$, $Al_{66.5}Cr_{28.5}Si_5$ and $Al_{63}Cr_{27}Si_{10}$ cathodes used for deposition, respectively.

3.2. Impact of the Si-content on the oxidation behavior

SEM micrographs of fracture cross-section of AlCrN, $AlCrSi_{2.5}N$ and $AlCrSi_5N$ in the as-deposited state with a coating thickness of about 11 µm are shown in Fig. 1. While AlCrN has a fine-grained columnar structure, the Si-containing coatings exhibit a more glassy and featureless morphology resulting from their nanocomposite structure with an even smaller grain size. The DSC signals and corresponding mass changes during annealing in ambient air to 1460°C are presented in Figure 2. Additionally, X-ray diffractograms of powders annealed at selected temperatures (indicated by vertical lines in Fig. 2) are shown in Fig. 3. Additionally, a schematic showing the formation of the various phases as a function of temperature summarizing the results of the DSC/TG and the XRD experiments is presented in Fig. 4. In the as-deposited state, the AlCrN coating is stabilized in the thermodynamically metastable cubic phase, as it is typical for an Al/Cr ratio of 2.3 [6, 35]. $AlCrSi_{2.5}N$ and $AlCrSi_5N$ exhibit a nanocomposite microstructure with dual-phase (hexagonal and cubic) crystallites embedded in an a-Si_xN_y matrix [25]. The formation of the nanocomposite microstructure also resulted in a substantial grain refinement and a higher defect density reflected by broader diffraction peaks with lower intensity and hence a noisier signal of the normalized diffractograms at RT in Fig. 3. Up to 1100°C, the only reactions taking place are recovery processes and the decomposition of the thermodynamically metastable c-AlCr(Si)N into the more stable h-Al(CrSi)N phase and a Cr-enriched c-Cr(AlSi)N phase. While recovery processes result in peaks with increasing intensity and decreasing FWHM with increasing annealing temperature, the formation of h-Al(CrSi)N is evidenced by an increased intensity of the reflections stemming from the hexagonal phase (Fig. 3). The contribution of both of these reactions to the DSC signal is relatively small compared to the oxidation processes at higher temperatures and hence results in only marginal buckles between 800°C and 1100°C in Fig. 2(a). A more detailed description of processes related to thermal stability excluding oxidation can be found in our previous paper [25].

A distinct deviation of the DSC signal from the baseline at 1100°C for AlCrN marks the onset of oxidation for the coating without Si. An evidence of oxidation detected also by XRD is visible at 1200°C in Figure 3a, where signals of Cr_2O_3 and Al_2O_3 emanate at 34° and 35°, respectively. The onset of oxidation is shifted to 1260°C for both Si containing coatings, indicated by the exothermic contribution to the DSC signal in Fig. 2(a). The oxidation of $AlCrSi_{2.5}N$ and $AlCrSi_5N$ proceeds relatively slowly up to 1300°C, as indicated by a shallow increase of the DSC signal and very small

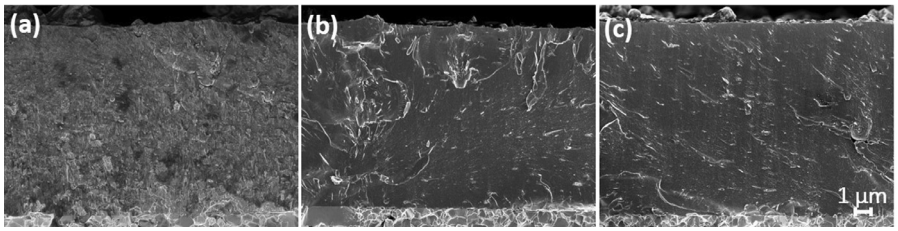

Fig. 1. SEM fracture cross-section images of (a) AlCrN, (b) AlCrSi2.5N and (c) AlCrSi5N coatings on a WC-Co substrates.

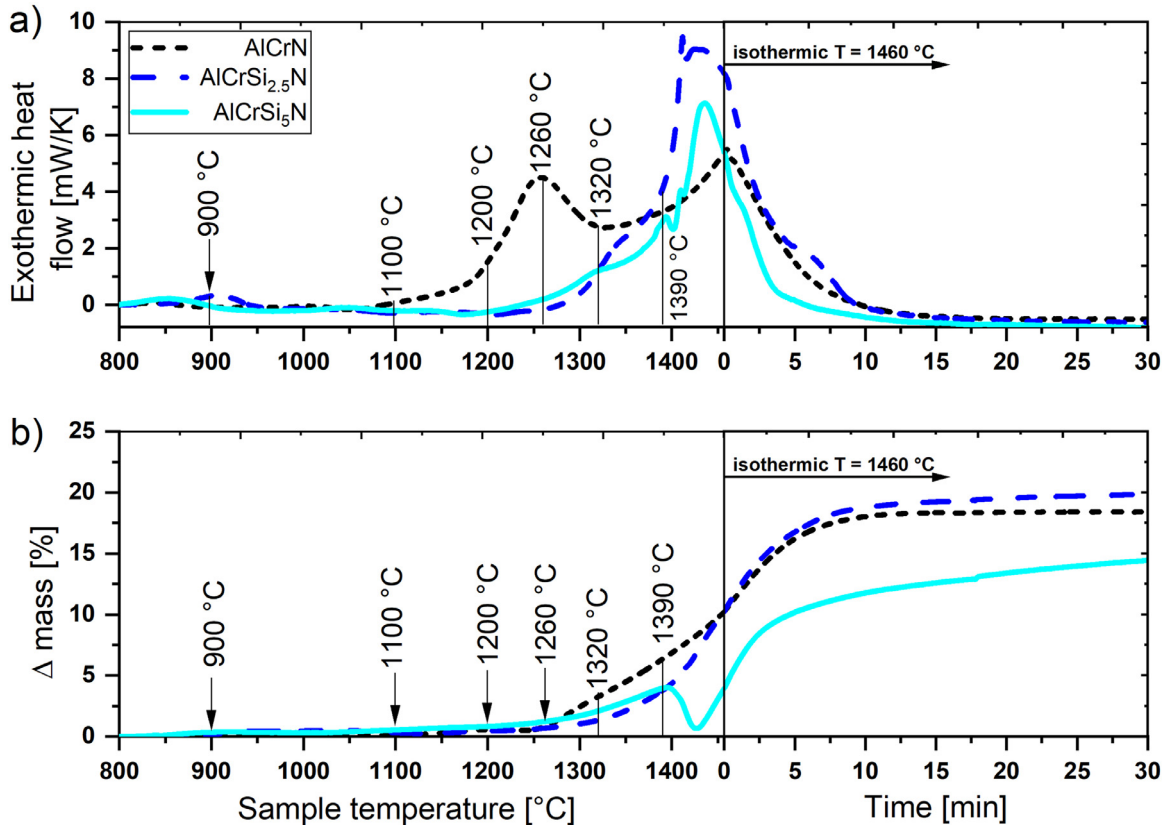

Fig. 2. (a) DSC and (b) TG curves of AlCrN, $AlCrSi_{2.5}N$ and $AlCrSi_5N$ coating powders in synthetic air. Annealing temperatures for ex-situ XRD measurements of powders are given.

peaks of oxide phases at 1320°C in Fig. 3(b) and (c). Additionally, peaks corresponding to the Cr_2N phase at 40.2° and 43.6° emanating at 1200°C in the X-ray diffractograms of all coatings reveal the decomposition of Cr-rich Cr(AlSi)N into Cr_2N, accompanied by the release of nitrogen. The nitrogen release partially compensates for the mass gain during oxidation, resulting in an almost constant mass signal up to 1260°C in Fig. 2(b). A large exothermic contribution to the DSC signal with a maximum at 1260°C for AlCrN (Fig. 2(a)) can be related to the formation of h-Al(CrSi)N and accelerated oxidation of the coating. The latter is demonstrated by an increasing sample mass above 1260°C (Fig. 2(b)). The oxidation of $AlCrSi_{2.5}N$ and $AlCrSi_5N$ accelerates at 1300 C as evidenced by a kink in the DSC signal (Fig. 2(a)), a pronounced mass gain (Fig. 2(b)) and an increasing contribution of the oxide phases to the X-ray diffractograms (Fig. 3(b) and (c)). Since Si_xN_y is not stable at temperatures above 1300°C in the presence of pure Cr, it decomposes and reacts with Cr while forming Cr_3Si [36]. This endothermic reaction leads to the buckles in the DSC signal obtained for $AlCrSi_{2.5}N$ and $AlCrSi_5N$ at ~1400°C, as shown in Fig. 2(a). Additionally, the subsequent release of nitrogen results in a considerable mass loss for $AlCrSi_5N$ at 1400°C (Fig. 2(b)). The Cr_3Si phase formed in $AlCrSi_{2.5}N$ and $AlCrSi_5N$ above 1390°C is also detected by XRD with peaks emanating at 39.5° and 44.3° (Fig. 3(b) and (c)).

During the isothermal holding period at the maximum temperature of 1460°C, the heat ow declines and converges to zero, which indicates a deceleration of the oxidation processes. While the AlCrN coating is fully oxidized after the annealing in ambient air (Fig. 3(a)), oxidation processes are still not completed for $AlCrSi_{2.5}N$ and $AlCrSi_5N$ (Fig. 3(b) and (c)). These findings are supported by the TG analysis (Fig. 2(b)). While the mass of the AlCrN sample remains unchanged after 10 min of annealing at 1460°C, the Si containing coatings changed their mass during the whole isothermal holding period (Fig. 2(b)). The uncomplete oxidation of the Si-containing coatings is also confirmed by XRD, where small fractions of h-Al(CrSi)N are still observed at 1460°C (Fig. 3(b) and (c)). After annealing at the maximum temperature of 1460°C, AlCrN consists only of an $(Al/Cr)_2O_3$ phase, while $AlCrSi_{2.5}N$ and $AlCrSi_5N$ are composed of a small h-Al(CrSi)N fraction and Al_2O_3, Cr_2O_3, SiO_2 and aluminosilicate phase (e.g. mullite, $3Al_2O_3{\bullet}2SiO_2$). While evenly shaped peaks located between the nominal peak positions corresponding to Al_2O_3 and Cr_2O_3 are visible for AlCrN (Fig. 3(a)), peak splitting of the reflections stemming from the oxide indicates

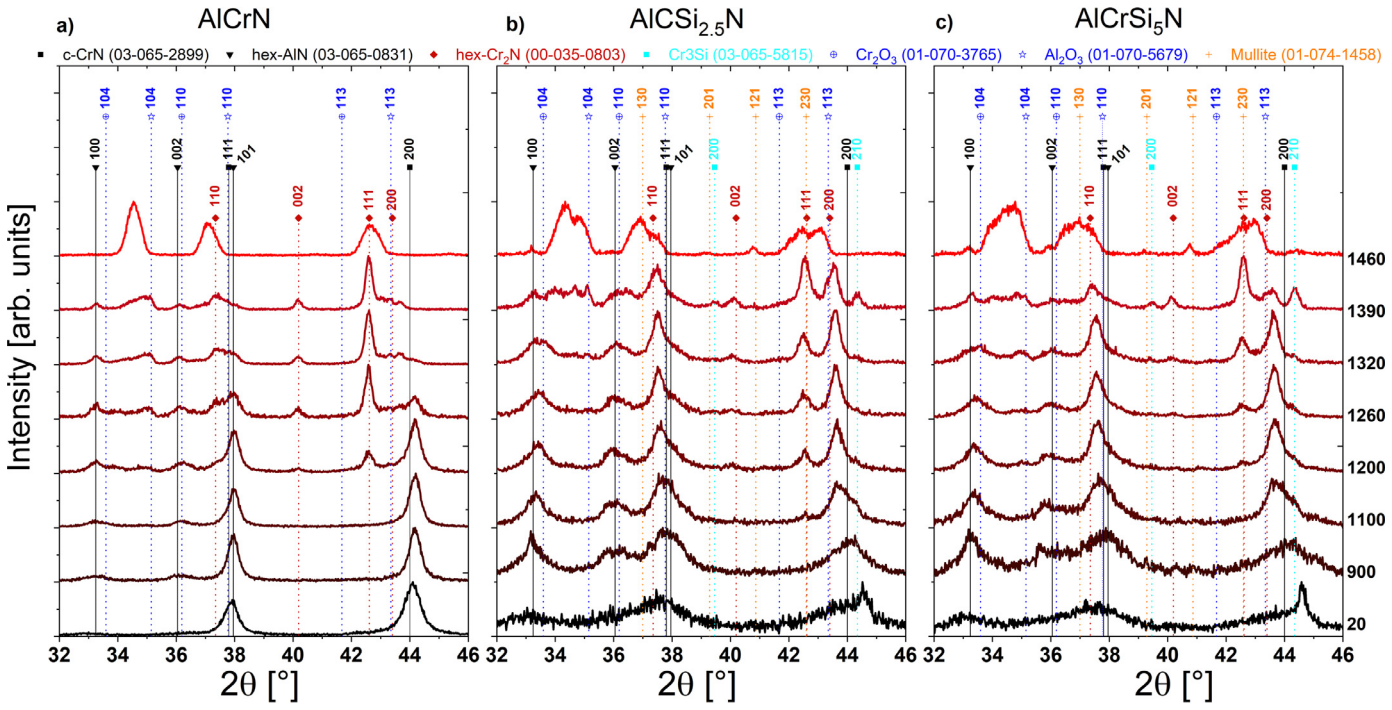

Fig. 3. X-ray diffractograms of (a) AlCrN, (b) $AlCrSi_{2.5}N$ and (c) $AlCrSi_5N$ coatings in the as-deposited state and after annealing at various temperatures in ambient air. Diffractograms with extended 2 angle are given in the supplementary Figure A.2 showing more details about the oxides formed in the Si-containing coatings after the DSC/TG experiment at 1460°C.

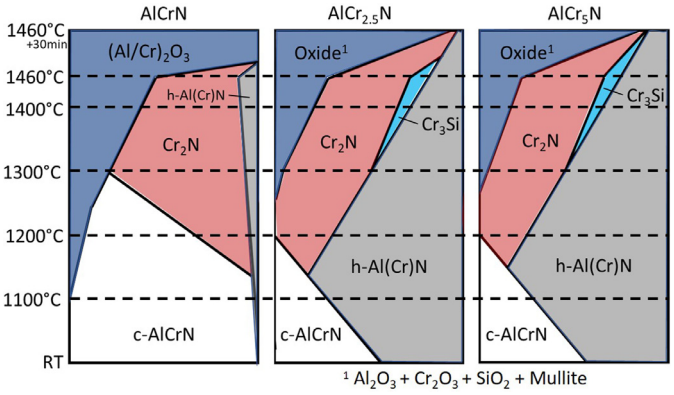

Fig. 4. Evolution of phases of AlCrN, $AlCrSi_{2.5}N$ and $AlCrSi_5N$ coatings as a function of temperature.

a separation into Al-rich and Cr-rich oxide phases for $AlCrSi_{2.5}N$ and $AlCrSi_5N$. The formation of the various phases as a function of temperature of the AlCrN, $AlCrSi_{2.5}N$ and $AlCrSi_5N$ coatings is summarized in Fig. 4, illustrating the main differences in phase evolution during oxidation. While AlCrN is purely cubic in the as-deposited state, the Si-containing coatings exhibit a dual phase hexagonal and cubic structure, also resulting in a diminished formation of Cr_2N at elevated temperatures. Finally, $AlCrSi_{2.5}N$ and $AlCrSi_5N$ benefit from the formation of Cr_3Si and an oxide layer comprising Al_2O_3, Cr_2O_3, Si_xO_y and some aluminosilicate, which results in overall reduced oxidation up to 1460°C.

3.3. Cross-sectional characterization of a partially oxidized $AlCrSi_5N$ coating

To better understand local elemental and structural changes occurring during oxidation, a partially oxidized sample of $AlCrSi_5N$ was studied depth-resolved across the coating thickness by cross-sectional X-ray nanodiffraction and TEM. $AlCrSi_5N$ was selected as it showed the highest oxidation resistance during DSC/TG investigations. Due to its outstanding oxidation resistance, the coating had to be annealed at 1400°C for 60 min in ambient air to induce oxidation to an extent, which allowed for formation of an oxide layer with sufficient thickness for further investigations. The partially oxidized sample consisted of an about 1.1 µm-thick oxide layer with a 3 µm-thick non-oxidized coating underneath (Fig. 5(a)).

3.3.1. Cross-sectional X-ray nanodiffraction

In Fig. 5, a cross-sectional SEM micrograph of the partially oxidized $AlCrSi_5N$ coating is shown together with the evolution of phases, residual stress and the FWHM as a function of coating depth. Throughout the coating, three zones developed differing in their composition and structure: at the very top, a dense oxide layer with a thickness of about 1.1 µm formed, followed by a 1 µm thick transition zone with incomplete oxidation. Finally, a non-oxidized 2 µm-thick zone close to the substrate with some pores is formed.

The oxidation progress across the coating depth is documented by the elemental variations across the coating thickness shown in Figure 5a. The oxygen content of the oxide layer is between 55 at.% and 66 at.%, strongly decreasing throughout the transition zone reaching a minimum of about 7 at.% in the non-oxidized coating. Simultaneously, while almost no nitrogen is present in the oxide layer, the nitrogen content rises to about 35 at.% within the transition zone and is then constant for the non-oxidized coating underneath. The oxide layer is separated into an Al-rich part at the very top with a thickness of 400 nm and a Cr-rich, 700 nm-thick part below. Hardly any Si except close to the surface (2 at.%) can be found in the oxide layer. While the Al-content increases within the transition zone to be constant at about 50 at.% for the non-oxidized coating, hardly any Cr can be found in the transition zone and the non-oxidized coating underneath. Only close to the substrate small amounts of Cr (2 at.%) can be found (Figure 5a). While an enrich-

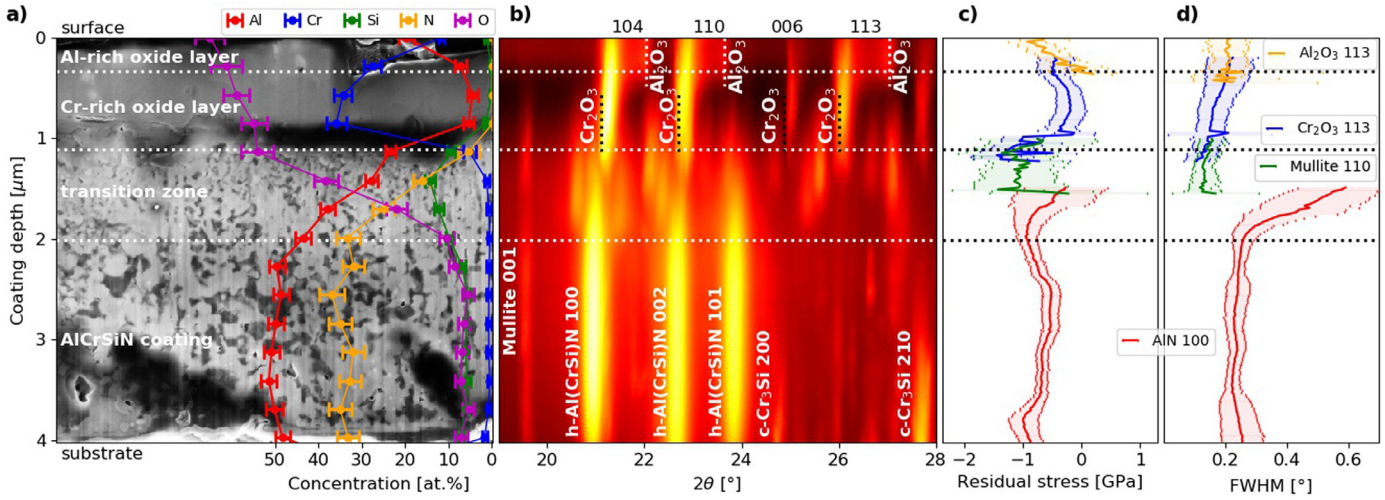

Figure 5. (a) SEM micrograph of the partially oxidized $AlCrSi_5N$ sample on a sapphire substrate (with included EDX line-scans), (b) phase evolution, (c) the residual stress development and (d) the FWHM values as a function of coating depth.

ment of Si in the transition zone with a maximum of about 15 at.% can be observed, it is constant for the non-oxidized coating at about 6 at.%.

The variation of the elemental composition is strongly related to the phase evolution and corresponds to the formation of the three zones differing in their phase composition and microstructure (Fig. 5(b)). The oxide layer is separated in Al_2O_3 at the very top and Cr_2O_3 underneath, both oxide phases exhibiting a trigonal crystal structure but a difference in their lattice constant. The transition zone below the oxide layer comprises numerous diffraction patterns with low intensity indicating the presence of phases varying in their elemental composition and oxidation state. They can be assigned to Al_2O_3, Cr_2O_3, mullite ($3Al_2O_3 \bullet 2SiO_2$), SiO_2 and AlN. Finally, the non-oxidized part of the coating consists mainly of the h-Al(CrSi)N phase with the absence of c-Cr(AlSi)N, Cr_2N or c-Cr. Some chromium silicide phases (mainly Cr_3Si, but also minor amounts of CrSi and Cr_5Si_3) can be found close to the substrate at a coating depth between 3 µm and 4 µm. These findings (together with the EDX measurement) suggest that the Cr almost completely diffused into the oxide layer at the very top of the coating during oxidation. In Figure 5c, the residual stress development across the coating depth evaluated from the AlN 100, the Cr_2O_3 and Al_2O_3 113 and the mullite 110 peak is depicted. The whole coating is compressively stressed with stresses ranging from -0.1 GPa to -1.5 GPa. A decrease of compressive residual stress with increasing distance from the surface from -1 GPa to -0.1 GPa is observed for Al_2O_3. The Cr_2O_3 phase exhibits a compressive stress of about -0.2 GPa, which is increasing to -0.6 GPa and -1.3 GPa towards the interfaces to the oxide layer and the transition zone, respectively. The highest compressive residual stress of the entire coating is found in the transition zone at about -1.1 GPa. Finally, the h-Al(CrSi)N phase is characterized by a constant compressive stress of -0.6 GPa for the major part of the non-oxidized coating, rising up to -1 GPa close to the transition zone and to the substrate.

In Fig. 5(d), the FWHM is plotted as a function of coating depth. The FWHM of an X-ray diffraction peak correlates with the crystallite size and stress of second and third order [37] and its changes, thus attributed to microstructural variations across the coating thickness. The Al_2O_3, the Cr_2O_3 and the mullite phase exhibit FWHM values decreasing from 0.2° to 0.1° with increasing distance from the surface. FWHM values up to 0.6° for the h-Al(CrSi)N phase within the transition zone decreasing to 0.2° and being constant at this value for the non-oxidized coating indicate a smaller grain size of the transition zone compared to the non-oxidized coating underneath.

3.3.2. TEM analysis of partially oxidized $AlCrSi_5N$

For a better understanding of the microstructural and elemental variations along the cross-section of the partially oxidized $AlCrSi_5N$ coating, STEM investigations including qualitative EDX measurements were performed. An overview of the sample cross-section by high-angle annular dark eld (HAADF) STEM is shown in Fig. 6(a), together with EDX mappings from selected areas at a higher magnification (Fig. 6(b-d)). From top to bottom, three different zones of the coating can be clearly distinguished: a dense oxide layer at the very top, a transition zone between the fully oxidized and non-oxidized part of the coating and a non-oxidized $AlCrSi_5N$ coating at the bottom (Fig. 6(a)). The oxide layer consists of an Al-rich layer (darker) and a Cr-rich layer below (brighter). The contrast can be referred to elements differing in their mass (atoms with higher atomic mass appear brighter). The elemental distribution of the oxide layer as determined by EDX (Fig. 6(b)) reveals an Al-rich oxide layer with slightly lower oxygen content at the very top of the coating and an oxide layer consisting almost exclusively of Cr-oxide with a higher amount of oxygen underneath. A Si-rich domain containing hardly any Al and Cr and with less oxygen compared to the surrounding Al and Cr oxide phases can be found between the Al-rich and Cr-rich oxide layers (Figure 6b). An abrupt change in the composition from a high oxygen content towards a very low oxygen- and a high nitrogen-content indicates the interface between the oxide layer and the transition zone underneath. Besides the different composition, the transition zone is characterized by a slightly finer grained microstructure. A pronounced segregation of Al and Si during annealing resulted in the formation of Al- and Si-rich domains. Further-more, the transition zone is strongly depleted of Cr, which is obviously concentrated only in macroparticles stemming from the deposition process. The non-oxidized coating underneath the transition zone exhibits a coarser grained microstructure, with an elemental composition similar to the one of the transition zone (Fig. 6(c)). Cr in this region can be found also exclusively in macroparticles, which exhibit an increased amount of oxygen compared to the surrounding coating. During annealing, Al- and Si-rich domains were formed. Additionally, pores (originating from the N-release during decomposition of CrN into Cr_2N) surrounded by a dark, grey rim can be clearly seen in the HAADF STEM micrograph (Fig. 6(d)). The rim of the pores is characterized by a low Al-, Cr- and N-content and consists mainly of Si and O.

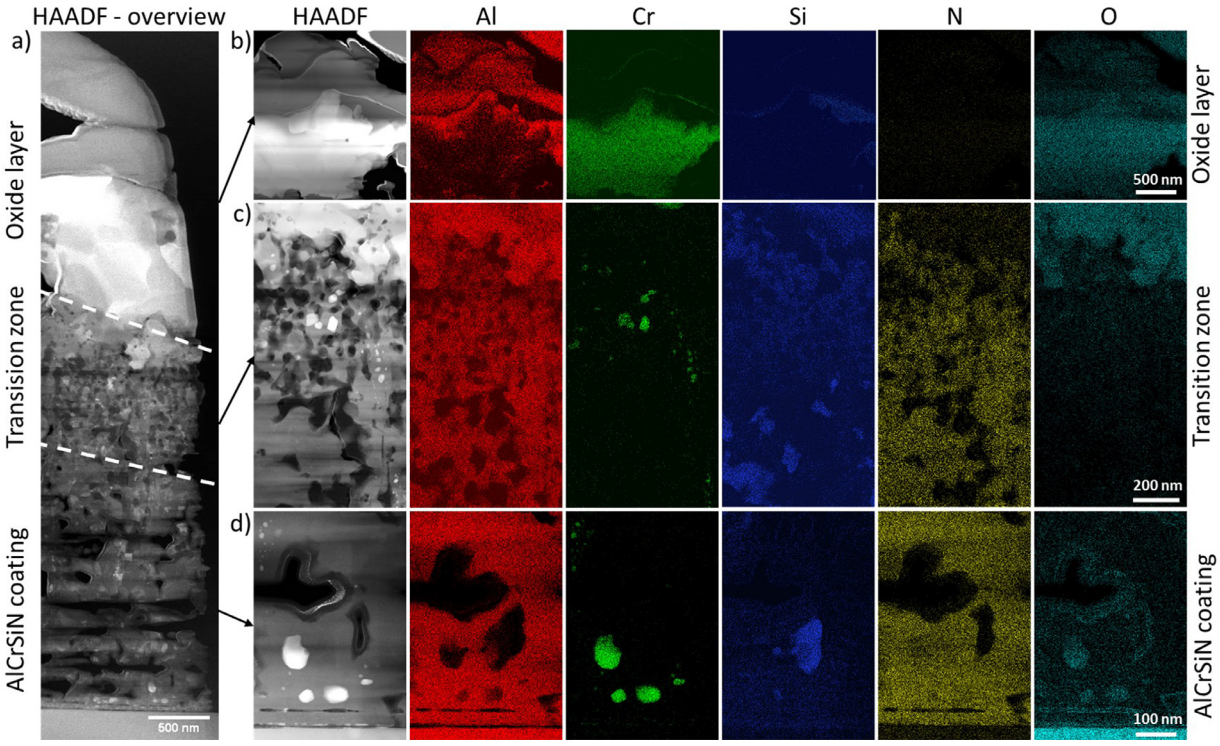

Fig. 6. STEM micrographs of the partially oxidized $AlCrSi_5N$ coating showing (a) an overview across the coating thickness as imaged by HAADF and EDX maps of (b) the oxide layer, (c) the transition zone and (d) the non-oxidized coating.

4. Discussion

The oxidation resistance of ceramic hard coatings at high temperatures depends not only on their elemental composition but is also strongly affected by their crystallographic phases and their microstructure. The latter have a major impact on the oxidation behavior as oxidation is a highly diffusion-controlled process. Physical vapor deposited coatings typically exhibit a columnar grain structure with elongated grains perpendicular to the substrate surface resulting from the competitive grain growth and thus suffer from continuous diffusion paths along the grain boundaries directly connecting surface and substrate, a downside which can be overcome by an advanced microstructural design like multi-layered architectures or amorphous grain boundary phases [38]. Two main diffusion-related mechanisms are decisive for high-temperature oxidation: (i) the relative outward diffusion of coating elements, like Al, Cr, Si and N for the coatings in this work, and (ii) the relative inward diffusion of oxygen. The diffusion of substrate elements across the coating-substrate interface may also play a role but is neglected here as only powders and coatings on thermally highly stable sapphire substrates were investigated. In applications, outwards diffusion of metallic elements from metal-based substrates may affect the oxidation kinetics, phase transformations and changes in the microstructure [39], which could be addressed by applying a diffusion barrier layer (e.g. TiN) between substrate and coating. The formation of an oxide layer on the top of the coating during early stages of oxidation strongly affects the inward diffusion of oxygen as well as the outward diffusion of coating elements. In general, elements forming dense oxide layers at the surface of the coatings are preferable as they act as protective passivation layers. An example is the improved oxidation resistance of AlCrN compared to CrN coatings, which is associated with the formation of an Al-rich oxide layer inhibiting the inward diffusion of oxygen [15]. The addition of Si also has a beneficial effect on the oxidation behavior of AlCr(Si)N coatings. Referring to the coatings investigated in this work, the onset of oxidation is shifted to higher temperatures from 1100°C to 1260°C for the Si-containing coatings compared to AlCrN, and the oxidation progress in the temperature range from 1200°C to 1460°C is slowed down significantly (Fig. 2 and Fig. 3). Si, like Al, forms dense, stable oxides as well and SiO_2 can be found in both oxidized Si-containing coatings (Fig. 3 and Fig. A.2). Additionally, SiO_2 and Al_2O_3 form stable chemical compounds with much lower enthalpy of formation (e.g. $\Delta H_{\text{mullite}}{}^0 = 6819$ kJ mol^{-1}) than Al_2O_3 ($\Delta H_{\text{Al}}{}^0 = 1676$ kJ mol^{-1}), Cr_2O_3 ($\Delta H_{\text{Cr}}{}^0 = 1140$ kJ mol^{-1}) or SiO_2 ($\Delta H_{\text{SiO}}{}^0 = 911$ kJ mol^{-1}) [40]. Therefore, an oxide layer tends to form in early stages of oxidation inhibiting the inward diffusion of oxygen and thus slowing down the subsequent oxidation process. Since the addition of Si to the AlCrN-system also results in the nanocomposite structure and the a-Si_xN_y grain boundary phase accompanied by a considerable grain refinement and densification of the microstructure (Fig. 1), inward diffusion of oxygen and outward diffusion of coating elements is further reduced as no continuous diffusion path along grain boundaries does exist anymore in contrast to the columnar microstructure of AlCrN [41]. This is also evident in the SEM micrographs of the powdered coatings after annealing at 1260°C given in the supplementary Fig. A.1. The surface morphology of areas where the top oxide layer chipped o allows for conclusions about the oxidation progress of the respective coatings. While the relatively rough surface morphology of AlCrN indicates that oxidation took place below the oxide layer too (Fig. A.1a), the comparatively smooth surface morphology of the Si-containing coatings indicates a limitation of the oxidation process to a thin oxide layer at the top, protecting the coating underneath (Fig. A.1b, c).

Another aspect in influencing the oxidation behavior of the respective AlCr(Si)N coatings is the thermal stability of the individual phases of the AlCr(Si)N coatings. In general, thermally stable phases are preferable compared to those with undergoing

phase transformations at elevated temperatures (e.g. c-AlCrN into h-AlCrN) as changes in crystal structure are typically accompanied by volume changes resulting in new diffusion paths associated with a higher defect density or even formation of microcracks [42, 21]. The crystallographic structure of AlCrN strongly depends on the Al/Cr ratio and can be stabilized in the thermodynamically metastable supersaturated face centered cubic solid solution phase up to an Al-content of 70 at.% on the metallic sublattice [6, 35]. For higher Al-contents the hexagonal dense packed structure becomes more favorable. Si also promotes the formation of the hexagonal phase [25]. Since the coatings investigated in this work have an Al/Cr ratio close to the cubic-to-hexagonal transition, AlCrN is the only purely cubic coating while $AlCrSi_{2.5}N$ and $AlCrSi_5N$ exhibit a mixed hexagonal and cubic structure due to the additional Si (Figure 3). Due to the metastable nature of the c-AlCr(Si)N phase, it starts to decompose into Cr-rich c-Cr(AlSi)N and Al-rich h-Al(CrSi)N phases [25]. The formation of the hexagonal AlN phase is accompanied by a volume expansion of 26 % [43], which results in the above-mentioned new diffusion paths. As this occurs to a much smaller extent for the Si-containing coatings (large amount of the hexagonal phase already present in the as-deposited state, Fig. 3) and the individual crystallites are embedded in the a-Si_xN_y matrix, $AlCrSi_{2.5}N$ and $AlCrSi_5N$ are much less affected by these phase changes at elevated temperatures and the oxidation progress is slowed down compared to AlCrN.

At even higher temperatures, the Cr-enriched c-Cr(AlSi)N phase starts to decompose into Cr_2N and finally into pure Cr, accompanied by the release of nitrogen [7]. These decomposition processes strongly affect the oxidation behavior in three different ways. Firstly, the release of nitrogen results in the formation of pores (Fig. 5 and Fig. 6) which facilitates enhanced diffusion (as surface diffusion is faster than bulk diffusion). Secondly, CrN has lower oxidation rates than those observed for Cr_2N [44]. The higher onset temperature and retarded progress for the decomposition of c-Cr(AlSi)N into Cr_2N and nitrogen, as shown in our previous work [25] and indicated by the X-ray diffractograms in Fig. 3, therefore also contributes to the enhanced oxidation resistance of the Si-containing coatings. Finally, free, unbound Cr, as the nal decomposition product, plays a major role in the oxidation process, as it was found to be more mobile compared to Al and thus di uses faster to the surface where it forms surface oxides [45]. While Cr in AlCrN can easily di use to the surface where it forms Cr_2O_3, free Cr is limited in the Si-containing coatings as it is bound in form of Cr_3Si (Fig. 3). Cr_3Si, as a chemical compound, can be assumed to have a much lower diffusivity than pure Cr, and thus outward diffusion of Cr is suppressed for the $AlCrSi_{2.5}N$ and $AlCrSi_5N$ coatings and the oxidation is slowed down. These findings are supported by X-ray reflections stemming from the Cr_3Si phase (at 2 angles of 24.7° and 27.7° in Fig. 5). The decreasing intensity of the X-ray reflections with increasing distance from the substrate towards the surface indicate that the outward diffusion of Cr is not fully completed yet and the Cr_3Si phase suppresses the diffusion.

The reduced Cr outward diffusion of the Si-containing coatings also affects the microstructure of the formed oxide layer. Usually, oxide layers with multi-layered structure are observed for AlCrN coatings [15, 46, 47]. Because of the higher mobility of Cr compared to Al, a Cr-rich oxide layer forms at the very top and an Al-rich oxide layer underneath. If the outward diffusion of Cr is prevented, for example by applying a TiN diffusion barrier as shown by Galindo et al. [45], the oxidation resistance of AlCrN coatings can be significantly enhanced. In the case of the Si-containing coatings of this work, the outwards diffusion of Cr is also strongly suppressed (as the free Cr is bonded to Si forming Cr_3Si which reduces its diffusion rate). As a result, a beneficial Al-rich oxide layer formed at the very top of the surface of the $AlCrSi_5N$ coating after annealing at 1400°C for one hour (Fig. 6, Fig. 5(b)), which is in contrast to AlCrN coatings of previous works where typically a Cr-rich oxide layer forms at the very top of the coatings [15, 46, 47].

The different oxidation behavior of the AlCr(Si)N coatings (suppressed outwards diffusion of Cr) also results in the formation of different oxides at the top of the coatings. While a mixed $(Al/Cr)_2O_3$ phase is observed for AlCrN, a separation into an Al_2O_3 and a Cr_2O_3 oxide is observed for $AlCrSi_{2.5}N$ and $AlCrSi_5N$ (Fig. 3). Although the Al_2O_3-Cr_2O_3 system exhibits a distinctive miscibility gap below 1300°C [48], a solid solution of those oxides formed on AlCrN during oxidation at 1460°C and sustained during cooling to room temperature was found (Fig. 3). In contrast, the Additionally formed SiO_2 in the Si-containing coatings is highly soluble in Al_2O_3 [49] but not soluble in Cr_2O_3 in the whole temperature range [50]. This is the reason why Al_2O_3 and Cr_2O_3 separated and coexist in the oxide layer, as indicated by separated peaks emanating from each phase (Fig. 3).

The annealing of the $AlCrSi_5N$ sample at the exceptional high temperature of 1400°C for 60 min in ambient air resulted in considerable diffusion of the respective coating elements, as-sociated by the formation of an oxide layer and substantial phase changes of the non-oxidized coating underneath. Despite these extensive elemental and microstructural changes, a com-pressive residual stress state is preserved for the whole coating (Fig. 5(c)) emphasizing the high thermal stability of the coating. The variations in the residual stress between -0.1 GPa and -1.5 GPa may originate from the thermal mismatch between the individual coating phases and/or coherency stresses between the different phases. Accordingly, the highest compressive stress within the whole coating can be found in the transition zone comprising the most different phases. Furthermore, slight pileups of heightened compressive stress can be found at the interfaces between the oxide layer and the transition zone, the transition zone and the non-oxidized coating and the coating-substrate interface.

The separation of the oxide at the top of the coating into phases with different elemental composition is accompanied by the formation of layers with different microstructures. While the Al-rich oxide layer seems to be finer grained (slightly larger FWHM in Fig. 5(d)), the Cr-rich oxide and the mullite is a little bit coarser grained (indicated by smaller FWHM in Fig. 5(d)). The Al(CrSi)N phase in the transition zone representing the oxidation front is relatively fine-grained as a result of the ongoing nucleation and formation of the oxide phases. The grain size increases towards the non-oxidized coating underneath and is constant for the 2 µm thick part of the coating close to the substrate. The originally nanocomposite structure of the non-oxidized coating underneath has changed in favor of a relatively coarse-grained microstructure. The coating elements strongly segregated and formed grains with individual high Al- and Si-content, while the Cr almost completely diffused to the top of the coating forming Cr_2O_3.

Summarized, Si has a beneficial impact on the oxidation behavior of the AlCrN-system already at relatively small concentrations up to 5 at.%. Higher Si-contents might further enhance the oxidation resistance but at the expense of a reduced hardness resulting from the larger fraction of the a-Si_xN_y phase [51]. The main impact on the oxidation behavior must be associated with the change in microstructure. While AlCrN has a two-dimensional microstructure with columnar grains allowing oxygen to di use along the grain boundaries, the addition of Si results in a three-dimensional nanocomposite microstructure where the AlCr(Si)N crystallites are embedded in an a-Si_xN_y tissue phase. The improved oxidation resistance of AlCrSiN coatings combined with their enhanced mechanical properties at high-temperatures (see our previous work [25]), makes the AlCrSiN coatings a perspective material for challenging high-temperature applications like high-speed or dry cutting.

5. Summary and conclusion

The oxidation behavior of arc evaporated AlCrN, $AlCrSi_{2.5}N$ and $AlCrSi_5N$ (fixed Al/Cr ratio of 70/30) was investigated by DSC/TG combined with ex-situ XRD. Additionally, a partially oxidized $AlCrSi_5N$ sample consisting of a 1.1 µm thick oxide layer on a 3 µm non-oxidized coating was cross-sectiofinally studied with respect to its elemental distribution, microstructure, formed phases and residual stress development by X-ray nanodiffraction and STEM. The beneficial effects rising from the addition of Si to the AlCrN-system can be summarized as follows:

- Formation of a nanocomposite structure with a dense a-Si_xN_y grain boundary phase avoiding continuous diffusion paths along grain boundaries from the coating surface to the substrate.
- Pronounced grain refinement and densification of the microstructure.
- Retarded decomposition of CrN into Cr_2N and thus retarded formation of pores due to the released nitrogen.
- Diminished diffusion of chromium outwards due to the formation of Cr_3Si leading to a favored Al-rich oxide layer at the very top of the coating preventing oxygen from diffusing inward.
- formation of dense, stable oxides (e.g. Si_xO_y and aluminosilicate) already during early stages of oxidation acting as passivation layers and slowing down oxidation

Cross-sectional X-ray nanodiffraction and STEM analysis after annealing an $AlCrSi_5N$ sample at 1400°C for one hour revealed a partially oxidized coating consisting of a 1.1 µm thick oxide layer, a 1 µm thick transition zone below and a 2 µm thick non-oxidized coating below. The oxide layer is divided into an Al-rich part at the very top and a Cr-rich part underneath. The transition zone represents the area of ongoing oxidation and exhibits a finer grained microstructure. Finally, a 2 µm thick non-oxidized coating is still remaining, represented by completely segregated coating elements into individual grains and some pores.

Adding Si to the AlCrN-system results in the formation of a self-assembling nanocomposite microstructure with highly beneficial properties. This advanced microstructural design al-lows for controlling the diffusion paths of oxygen and coating elements through the coating and for governing the microstructure of the oxidation layer formed at the top protecting the coatings from further oxidation. As a result, the onset of oxidation was increased from 1100°C to 1260°C and the speed of the oxidation was slowed down significantly, which makes AlCrSiN coatings promising candidates for high-temperature applications such as high-speed or dry cutting.

Declaration of Competing Interest

The authors declare that they have no known competing financial interests or personal relationships that could have appeared to influence the work reported in this paper.

Acknowledgments

The work has been financially supported by Christian Doppler Research Association. The financial support by the Austrian Federal Ministry for Digital and Economic A airs and the National Foundation for Research, Technology and Development is gratefully acknowledged. The authors would also like to thank Ilse Letofsky-Papst (Austrian Centre for Electron Microscopy and Nanoanalysis, Graz) for the STEM investigations.

Supplementary materials

Supplementary material associated with this article can be found, in the online version, at doi:10.1016/j.jmst.2021.04.065.

References

[1] G. List, G. Sutter, A. Bouthiche, Int. J. Mach. Tool. Manuf. 54-55 (2012) 1–9.
[2] E. Spain, J.C. Avelar-Batista, M. Letch, J. Housden, B. Lerga, Surf. Coat. Technol. 200 (2005) 1507–1513.
[3] L. Wang, X. Nie, J. Housden, E. Spain, J.C. Jiang, EI. Meletis, A. Leyland, A. Matthews, Surf. Coat. Technol. 203 (2008) 816–821.
[4] Y. Benlatreche, C. Nouveau, R. Marchal, J.P.F. Martins, H. Aknouche, Wear 267 (2009) 1056–1061.
[5] T. Polcar, A. Cavaleiro, Surf. Coat. Technol. 206 (2011) 1244–1251.
[6] M. Kawate, A. Kimura, T. Suzuki, J. Vac. Sci. Technol. A 20 (2002) 569–571.
[7] H. Willmann, P.H. Mayrhofer, P.O.A. Persson, A.E. Reiter, L. Hultman, C. Mitterer, Scripta Mater. 54 (2006) 1847-1851.
[8] M. Meindlhumer, S. Klima, N Jager, A. Stark, H. Hruby, C. Mitterer, J. Keckes, R. Daniel, Sci. Rep. 9 (2019) 18027.
[9] Y. Feng, L. Zhang, R. Ke, Q. Wan, Z. Wang, Z. Lu, Int. J. Refract. Met. Hard Mat. 43 (2014) 241–249.
[10] R. Forsen, MP Johansson, M. Oden, N. Ghafoor, Thin Solid Films 534 (2013) 394–402.
[11] Y. Chang, S. Weng, C. Chen, F. Fu, Surf. Coat. Technol. 332 (2017) 494–503.
[12] B. Xiao, J. Liu, F. Liu, X. Zhong, X. Xiao, T. Zhang, Q. Wang, Ceram. Int. 44 (2018) 23150–23161.
[13] N. Jager, S. Klima, H. Hruby, J. Julin, M. Burghammer, J.F. Keckes, C. Mitterer, R. Daniel, Acta Mater 162 (2019) 55–66.
[14] S. Klima, N. Jager, H. Hruby, C. Mitterer, J.F. Keckes, M. Burghammer, R. Daniel, Mater. Des. 170 (2019) 107702.
[15] A.E. Reiter, C. Mitterer, B. Sartory, J. Vac. Sci. Technol. A 25 (2007) 711–720.
[16] J.L. Endrino, V. Derflinger, Surf. Coat. Technol. 200 (1) (2005) 988–992 PSE 2004.
[17] T. Polcar, A. Cavaleiro, Surf. Coat. Technol. 205 (2011) S107–S110.
[18] R. Franz, J. Neidhardt, C. Mitterer, B. Schaffer, H. Hutter, R. Kaindl, B. Sartory, R. Tessadri, P.Polcik Lechthaler, J. Vac. Sci. Technol. A 26 (2008) 302–308.
[19] M.S. Dominguez-Meister, S. El Mrabet, R. Escobar-Galindo, A. Mariscal, M.C. Jimenez de Haro, A. Justo, M. Brizuela, T.C. Rojas, J.C. Sanchez-Lopez, Appl. Surf. Sci. 353 (2015) 504–511.
[20] F. Rovere, P.H. Mayrhofer, A. Reinholdt, J. Mayer, J.M. Schneider, Surf. Coat. Technol. 202 (2008) 5870–5875.
[21] C. Tritremmel, R. Daniel, C. Mitterer, P.H. Mayrhofer, M. Lechthaler, P. Polcik, J. Vac. Sci. Technol. A 30 (2012) 061501.
[22] J.L. Endrino, S. Palacin, A. Gutierrez, F. Schäffers, J.E. Krzanowski, J. Mater. Sci. 42 (2007) 7607–7610.
[23] J. Soldan, J. Neidhardt, B. Sartory, R. Kaindl, R. Cerstvy, P.H. Mayrhofer, R. Tessadri, P. Polcik, M. Lechthaler, C. Mitterer, Surf. Coat. Technol. 202 (2008) 3555–3562.
[24] J. Musil, P. Zeman, Solid State Phenomena 127 (2007) 31–36.
[25] N. Jager, M. Meindlhumer, S. Spor, H. Hruby, J. Julin, A. Stark, F. Nahif, J. Keckes, C. Mitterer, R. Daniel, Acta Mater 186 (2020) 545–554.
[26] J. Keckes, R. Daniel, J. Todt, J. Zalesak, B. Sartory, S. Braun, J. Gluch, M. Rosenthal, M. Burghammer, C. Mitterer, S. Niese, A. Kubec, Acta Mater 144 (2018) 862–873.
[27] C. Riekel, M. Burghammer, R. Davies, Progress in micro- and nano-diffraction at the ESRF ID13 beamline, IOP Conference Series: Materials Science and Engineering 14 (2010) 012013.
[28] A. Kubec, K. Melzer, J. Gluch, S. Niese, S. Braun, J. Patommel, M. Burghammer, A. Leson, J. Synchrot. Radiat. 24 (2017) 413–421.
[29] G. Ashiotis, A. Deschildre, Z. Nawaz, J.P. Wright, D. Karkoulis, F.E. Picca, J. Kieffer, J. Appl. Crystallogr. 48 (2015) 510–519.
[30] J. Kieffer, D. Karkoulis, Journal of Physics: Conference Series 425 (2013) 202012 2013.
[31] Y. Wang, H. Fang, C.L. Zacherl, Z. Mei, S. Shang, L. Chen, P.D. Jablonski, Z. Liu, Surf. Sci. 606 (2012) 1422–1425.
[32] B. Hildmann, H. Ledbetter, S. Kim, H. Schneider, J. Am. Ceram. Soc. 84 (2001) 2409–2414 2001.
[33] J. Almer, U. Lienert, R.L. Peng, C. Schlauer, M. Oden, J. Appl. Phys. 94 (2003) 697–702.
[34] I.C. Noyan, J.B. Cohen, Residual stress: measurement by diffraction and interpretation, Springer, 2013.
[35] A.E. Reiter, V.H. Derflinger, B. Hanselmann, T. Bachmann, B. Sartory, Surf. Coat. Technol. 200 (2005) 2114–2122.
[36] T. Shimoo, K. Okamura, J. Mater. Sci. 29 (1994) 2231–2237.
[37] E.J. Mittemeijer, U. Welzel, Cryst. Mater. 223 (2008) 552–560.
[38] J. Musil, Surf, Coat, Technol 207 (2012) 50–65.
[39] T.C. Rojas, S. Dominguez-Meister, M. Brizuela, J.C. Sanchez-Lopez, Surf. Coat. Technol. 354 (2018) 203–213 2018.
[40] John Aurie Dean, Lange's handbook of chemistry, 15, McGraw-Hill, New York, 1992.
[41] J. Musil, J. Vlcek, P. Zeman, Adv. Appl. Ceram. 107 (2008) 148–154.
[42] L. Hultman, Vacuum 57 (2000) 1–30.
[43] P.H. Mayrhofer, D. Music, J.M. Schneider, J. Appl. Phys. 100 (2006) 094906.
[44] T. Kacsich, K.P. Lieb, A. Schaper, O. Schulte, J. Phys.: Condens. Matter 8 (1996) 10703–10719.
[45] R.Escobar Galindo, J.L. Endrino, R. Mart nez, J.M. Albella, Spectrochim. Acta Part B 65 (2010) 950–958.
[46] S. Hofmann, H.A. Jehn, Werkstoffe und Korrosion 41 (1990) 756–760.
[47] Y. Ide, T. Nakamura, K. Kishitake, Formation of Al-Cr-N films by a DC reactive sputtering method and evaluation of their properties. In B. Mishra, Yamauchi

C, B. Mishra, and C. Yamauchi, editors, Proceedings of the Second International Conference on Processing Materials for Properties, 2000, pp. 291-296,
[48] W. Sitte, Materials Science Monographs 28 (1985) 451–456.
[49] N.L. Bowen, J.W. Greig, J. Am. Ceram. Soc. 7 (1924) 238–254.
[50] T.M. Besmann, N.S. Kulkarni, K.E. Spear, J. Am. Ceram. Soc. 89 (2006) 638–644.
[51] C. Tritremmel, R. Daniel, M. Lechthaler, P. Polcik, C. Mitterer, Thin Solid Films 534 (2013) 403–409.